BNL-108275-2015-JA

Structural Characterization of Highly Irradiated Reactor Pressure Vessel Steels

D. J. Sprouster,[1, a)] J. Sinsheimer,[2] E. Dooryhee,[2] S. Ghose,[2] P. Wells,[3] T. Stan,[3] N. Almirall,[3] G. R. Odette,[3] and L. E. Ecker[1]

[1)] *Nuclear Science and Technology Department, Brookhaven National Laboratory, PO Box 5000, Upton, NY 11973, USA*

[2)] *National Synchrotron Light Source II, Brookhaven National Laboratory, PO Box 5000, Upton, NY 11973, USA*

[3)] *Materials Department, University of California, Santa Barbara, CA 93106, USA*

(Dated: 15 June 2015)

Massive, thick-walled pressure vessels are permanent nuclear reactor structures that are exposed to a damaging flux of neutrons from the adjacent core. The neutrons cause embrittlement of the vessel steel that increases with dose (fluence or service time), as manifested by an increasing temperature transition from ductile-to-brittle fracture. Extending reactor life requires demonstrating that large safety margins against brittle fracture are maintained at the higher neutron fluence associated with 60 to 80 years of service. Here synchrotron-based x-ray diffraction and small angle x-ray scattering measurements are used to characterize a new class of highly embrittling nm-scale Mn-Ni-Si precipitates that develop in the irradiated steels at high fluence. These precipitates can lead to severe embrittlement that is not accounted for in current regulatory models. Application of the complementarity techniques has, for the very first time, successfully characterized the crystal structures of the nanoprecipitates, while also yielding self-consistent compositions, volume fractions and size distributions.

PACS numbers: 61.80.-x,61.05.C-, 75.50.Bb

[a)] dsprouster@bnl.gov

I. INTRODUCTION

Reactor pressure vessels (RPVs) are the primary permanent component of light water reactors (LWRs). RPVs experience irradiation embrittlement that increases with neutron fluence (see Refs[1–3] for overviews of the embrittlement phenomena and underlying mechanisms). Ensuring that large safety margins are maintained in the face of embrittlement is required to extend LWR service life to beyond 60 years. Embrittlement is marked by increases in the ductile-to-brittle transition fracture temperature (ΔT) of RPV steels. The ΔT is primarily caused by irradiation hardening ($\Delta\sigma_y$) associated with the formation of nm-scale precipitates and solute-defect complexes that act as obstacles to dislocation glide. At low to intermediate neutron fluence, significant hardening and embrittlement is primarily caused by the formation of coherent, transition phase copper rich precipitates (CRPs). Cu is insoluble in steels and rapidly phase separates due to radiation enhanced diffusion at RPV service temperatures (around 290 °C). The CRPs are also enriched in Mn, Ni and Si, in the form of a core (primarily Cu)-shell (primarily Mn-Ni-Si) structure. The hardening and embrittlement due to CRPs saturates when the trace amounts of Cu (< 0.35 at.%) are depleted from the ferrite matrix. However, the Mn, Ni and Si solutes continue to slowly accumulate at the precipitates and grow to large volume fractions at high fluence, since there is much more Mn + Ni + Si (typically $> 2.5\%$) than Cu in typical low alloy RPV steels. Further, it was long ago predicted[4–6] and more recently shown that Mn-Ni-Si precipitates (MNS) can also form in low or no Cu steels, but only at sufficiently high fluence[7–11]. Hence the MNS have also been called late blooming phases. The ΔT approximately scales as 300 °C $\times \sqrt{(volume fraction)}$[1,2,10]. Thus the large volume fractions associated with MNS could limit safe extended RPV lifetimes. However, late blooming MNS are not accounted for in current embrittlement regulatory models based on lower fluence databases.

Solute precipitation and embrittlement are complex phenomenon that depend on the *combination* of both metallurgical (microstructure, composition, product form and heat treatment) and irradiation (neutron flux, fluence, irradiation temperature) variables. RPV steels have a very wide range of compositions that may be vulnerable to MNS precipitation: Cu $\sim$ 0-0.35, Mn 0.8-1.6, Ni 0.2-1.6, Si 0.4-1.2 in at.%. Formation of MNS also depends on the irradiation temperature, flux and fluence. In general, MNS are promoted by higher Ni

and Cu, lower temperatures and flux and, as noted previously, high fluence. Thus there is a pressing need to incorporate MNS effects into embrittlement models that can reliably extrapolate ΔT predictions to extended life at high-fluence, low-flux service conditions, where little or no data currently exists. This requires robust physical models that are informed and calibrated by well-designed experiments and characterization studies.

The radiation-induced precipitation of MNS in RPV steels has primarily been studied by small angle neutron scattering (SANS) and atom probe tomography (APT). The APT studies provide good measures of MNS precipitate number densities (N), volume fractions (f) and size distributions (d) and show that their compositions lie in the vicinity of the G ($Mn_6Ni_{16}Si_7$) and Γ_2 (Mn_2Ni_3Si) phases in the Mn-Ni-Si ternary projection of the Fe-based quaternary system[10,12]. However, neither SANS or APT provides information on the crystal structure of MNS. Phase identification is needed to develop rigorous thermodynamic and kinetic precipitation models. However, characterizing MNS crystal structures is very difficult, due to their nm-scale sizes, complex chemistry and limited volume fractions[9,13]. In principle, transmission electron microscopy (TEM) can be used for structure identification, but this has had limited success indexing the G-phase in only a few cases.

Standard x-ray diffraction techniques suffer the same challenges in phase identification[14,15]. However, in this work, advanced synchrotron x-ray techniques successfully identified the MNS intermetallic phases in a set of six irradiated RPV steels with systematic variations in Cu and Ni contents. Phase identification is enabled by a combination of small angle x-ray scattering (SAXS) and x-ray diffraction (XRD). The corresponding results of the synchrotron x-ray techniques for MNS f and d are shown to be internally self-consistent and in good agreement with APT measurements.

II. MATERIALS AND METHODS

The chemical compositions of the six split melt RPV steels investigated are shown in Table 1. The alloys were irradiated to a high-fluence of 1.10 $\times 10^{21}$ n/cm^2 at 290 °C in the Idaho National Laboratory Advanced Test Reactor (ATR) at a neutron flux $\sim$ 2.3 $\times 10^{14}$ n/cm^2-s. Specimens in the form of 2×0.5 mm discs were wrapped in three layers of Kapton

to prevent any radioactive contamination at the synchrotron beamlines.

High-resolution XRD measurements were performed at the National Synchrotron Light Source using the high-energy X-rays available at beamline X17A. SAXS measurements were performed at the X-ray Powder Diffraction (XPD) beamline of the new National Synchrotron Light Source-II. All measurements were performed in transmission mode with an amorphous Silicon-based flat panel detector (Perken-Elmer) mounted orthogonal to and centered on the beam path. The sample-to-detector distances and tilts of the detector relative to the beam were refined using either a CeO_2 (XRD), or Silver Behenate (SAXS) powder standards. The wavelengths of the incident X-rays was 0.1839 Å(67.42 keV, X17A) and 0.2361 Å(52.51 keV, XPD). The sample-to-detector distances were calculated to be 780 mm (XRD) and 2893 mm (SAXS). Multiple patterns were collected to avoid saturation of the detector. Typical count times were 0.5-1 sec (depending on the sample). Each diffraction or scattering pattern consisted of the average of 100-500 individual exposures. All raw two-dimensional patterns were background corrected by subtracting the dark current image and Kapton/air scattering. Noticeable artifact regions of the detector (beam stop, dead pixels) were masked. The corrected and masked two-dimensional detector images were then averaged and radially integrated to obtain the one-dimensional powder diffraction and SAXS patterns.

The measured SAXS intensities were converted to absolute cross-section units following the methods described in Ref [16]. Particle sizes were determined using the nonlinear least square fitting procedures in the IGOR Pro-based software package IRENA[17]. Spherical particles were assumed, consistent with previous APT and TEM measurements[10]. The electron density difference (or atomic density difference) between the matrix and the particles were calculated within IRENA based on their respective bulk-phase values.

The XRD patterns were Rietveld refined with the TOPAS software package (BRUKER). The peak profiles were modeled by a modified pseudo-Voigt function. The instrument contribution to the broadening of the measured profiles was quantified by fitting a CeO_2 NIST powder standard (38 hkl reflections), with known crystalline-domain size and negligible strain contribution. The Gaussian and Lorentzian-based broadening parameters were subsequently fixed during the analysis of the alloys under investigation. The f, domain size,

lattice parameter and strain were allowed to vary during the Rietveld refinements, with the temperature factors nominally fixed to their bulk values taken from the literature[13,16,18–20]. The temperature factors were not allowed to vary due to their strong correlation with the weight fractions. The strain components for the small austenite fcc phase[21], the cementite (alloyed Fe_3C type phase) and MNS (described below) were not included in the refinements due to the known complications in quantifying strains in such small particles[22,23]. Furthermore, in the case of the irradiated alloys, where the diffraction contributions of the nm-scale MNS are small, the particle size, determined from SAXS, was fixed and only f and the lattice parameter were allowed to vary during the refinement. This method is similar to that employed in the field of mineralogy to determine the structure and fraction of a phase with partial or no known crystal structure (PONKCS)[24,25].

III. RESULTS AND DISCUSSION

A. Small-Angle X-ray Scattering

Figure 1 shows illustrative background corrected SAXS patterns for the (a) LD and (b) CM6 unirradiated and irradiated alloys. The scattering intensity at low-Q, is indicative of features with sizes of $\sim$ 40-70 nm, that can be attributed to the cementite particles. The SAXS patterns for all the alloys were found to change significantly following irradiation. Decreases in the scattering intensity were observed at very low-Q. The increase in the scattering amplitude at higher Q in the irradiated samples is due to the formation of new nm-scale MNS precipitates. The average d and f of these precipitates in the 6 alloys from the SAXS analysis is shown in Table 2. The MNS d and f quantified by SAXS agree very well with APT characterization results[10].

B. X-ray Diffraction

Figure 2 shows the XRD patterns for selected unirradiated and irradiated alloys with the identified phases superimposed for reference. The quantitative Rietveld results for the unirradiated samples are given in Table 3. The line broadening from the strain components

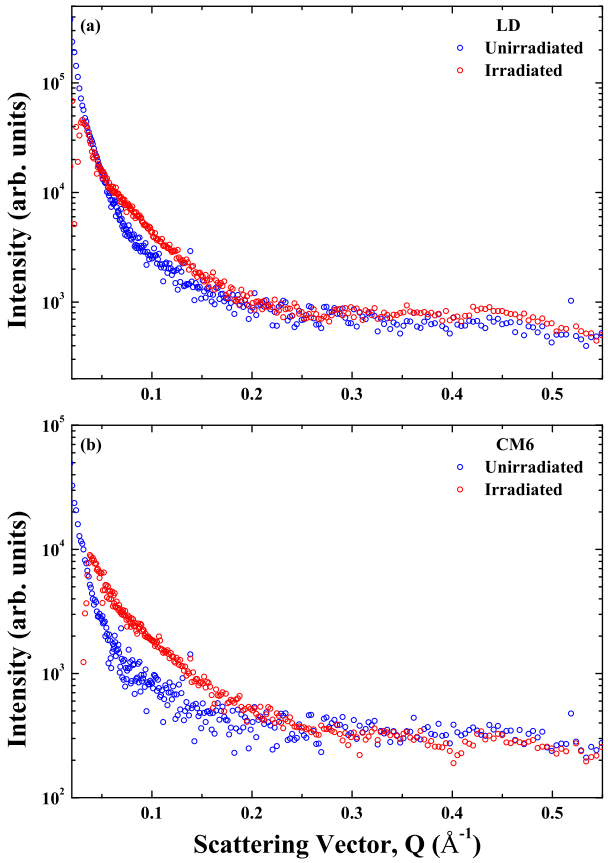

FIG. 1. Background corrected SAXS scattering intensity as a function of scattering vector, Q, for the irradiated LD and CM6 samples.

are small for the ferrite phase. All the unirradiated alloys also display a small fcc phase contribution. These small crystallites are primarily attributable to the austenite phase (fcc Fe), although, in some cases, there may be a small contribution from fcc Cu that precipitates during heat treatments[1]. The fraction, domain size and lattice parameters of the austenite crystallites determined from the Rietveld analysis are also given in Table 2.

Figure 2 shows those changes in the XRD patterns after irradiation include: a) an increase in the structured scattering background; b) a slight broadening of the ferrite and cementite peaks; and c) complete removal of the peaks associated with the fine scale austenite phase. The only alloys that retain an austenite component after irradiation were the LD and CM6, both with higher Ni contents. These alloys also initially contained the largest austenite crystallites prior to irradiation. The removal of the peaks associated with the retained austenite indicates that irradiation leads to their transformation to ferrite or a sig-

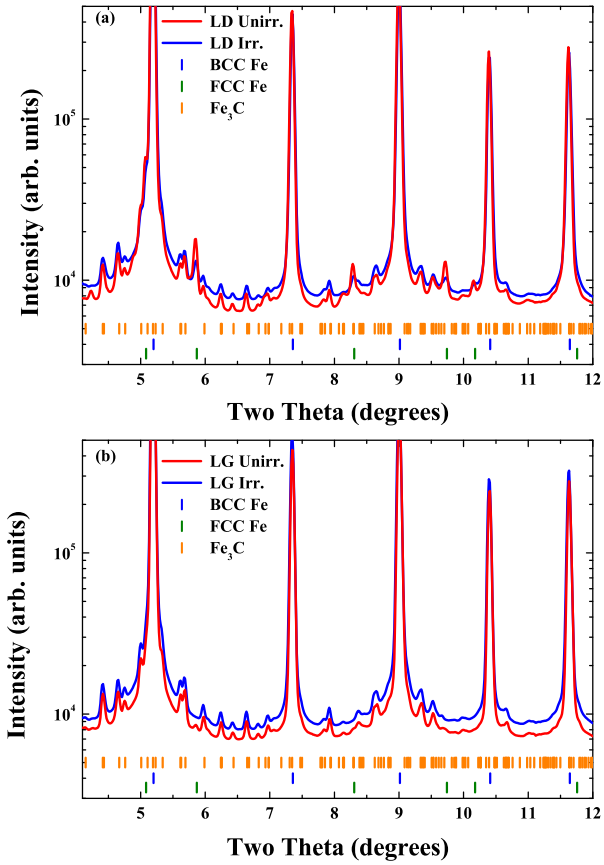

FIG. 2. High-resolution XRD patterns for the unirradiated and irradiated (a) LD (b) LG samples. The peaks attributable to the Cementite, Austenite and Ferrite phases are included for reference.

nificant decrease in their size (again for the LD and CM6), consistent with previous studies[26].

The quantitative Rietveld analysis of the irradiated alloys, given in Table 4, reveals that there are subtle changes in the crystalline domain size and an increase in the strain broadening in the ferrite phase compared to their unirradiated counterparts as summarized in Table 3. Since these length scales are much smaller than the prior austenite grain size in these alloys, the differences are attributed subgrain structures and extended defects such as dislocations and dislocation loops. The corresponding changes in the cementite phase following irradiation are more modest and less systematic. Notably, there is no strong diffraction signal from the MNS precipitates that are known to be present from the APT and SAXS measurements.

To obtain and quantify structural information on the MNS, the diffraction patterns were

simultaneously refined while incorporating both $Mn_6Ni_{16}Si_7$ and Mn_2Ni_3Si phases with fixed domain sizes that were previously determined from the SAXS and APT measurements. The only additional parameters allowed to vary in the refinements were the f and lattice parameters of the MNS phases. Figure 3 shows representative fits using the modified Rietveld method, again for the LD and CM6 alloys. The quantitative results for the MNS are given in Table 4. Only one MNS phase could be refined with confidence in each individual alloy, while the other phase consistently returned non-physical parameters and low f ($< 0.1\%$). Notably, the f from the refined XRD analysis are in excellent agreement with those determined from the APT[10] as well as the SAXS measurements described above. The lattice parameters determined from the Rietveld refinement are slightly different (averaging $\sim +1.8$ % for L-series alloys and $\sim$ -7.1% for the CM6 alloy) compared to their bulk counterparts ($Mn_6Ni_{16}Si_7$: 11.167 Å[13] and Mn_2Ni_3Si: 6.673 Å[12,27]), respectively. These differences may be due to the complex MNS chemistry in combination with the large surface-to-volume ratios of these nm-scale features embedded in the ferrite matrix, as has been observed in other comparable nanoparticle ensembles[28–30][31]. Further, in the L-series alloys, the deviations were on average significantly larger in the steels with MNS appended to CRP.

The phase selection in the Rietveld refinement analysis are also consistent with Thermocalc II database based thermodynamic predictions for the L-series high Ni high Cu alloy LD and the high Ni low Cu CM6 alloy, containing $Mn_6Ni_{16}Si_7$ and Mn_2Ni_3Si-phases respectively[11]. In both of these cases, the APT measurements also closely match the corresponding stoichiometric intermetallic phase compositions. However, the Thermocalc II database based thermodynamic model predicted a mix of $Mn_6Ni_{16}Si_7$ and Mn_2Ni_3Si-phases in the other irradiated intermediate Ni L-series alloys (LG, LH, LI, LC). Notably, the APT compositions of these alloys lie near the Si rich end of the Mn_2Ni_3-phase field. However, an alternative University of Wisconsin thermodynamic database predicted the formation of the Mn_2Ni_3Si-phase in all six alloys. Thus the combined SAXS/APT and refined XRD data provide a basis to test and improve the parameterization of the thermodynamic models in a way that is not possible using either technique alone. More generally, the XRD Rietveld refinements confirm the thermodynamic predictions that the MNS precipitates are indeed crystalline intermetallic phases[11].

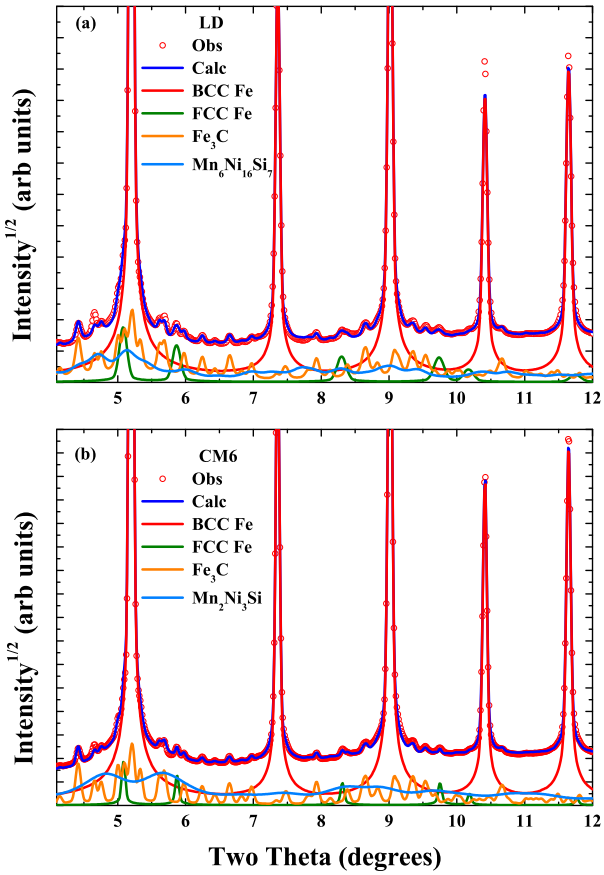

FIG. 3. Modified Rietveld refinements for the (a) LD and (b) CM6 irradiated samples. The components of each phase are included for reference.

It is important to recognize the occurrence and character of MNS phases has previously been a matter of considerable controversy[32,33]. It has been argued, mainly based on computer simulations, that such features were neither late blooming, in the sense that they evolve to large volume fractions at high fluence beyond a minimum threshold, or that they were phases at all, rather than being non equilibrium sub-nm solute-defect cluster complexes, likely formed in high recoil energy neutron induced cascades. Indeed, we believe that these cascade cluster complexes are likely precursors to well-formed MNS precipitates, but again the latter evolve only at high fluence. This controversy has been largely laid to rest by previous APT results and models such as those in[10,11]. However, the phase identification achieved in this study make the case even more compelling. More importantly the current results that show the intermetallic nature of MNS is extremely important to informing rigorous physically based thermodynamic and kinetic models of irradiation enhanced pre-

cipitation, and the resulting hardening and embrittlement of RPV steels. Such models are needed to more reliably extrapolate to conditions beyond the existing surveillance database.

IV. CONCLUSION

In summary, we have shown a combination of complementary characterization methods can be used to develop a more detailed understanding of embrittlement of RPV steels irradiated up to high neutron fluence. MNS sizes from SAXS and APT measurements were used in quantitative Rietveld refinements, yielding, for the first time, characterization of the crystal structures of intermetallic MNS phases in highly irradiated RPV alloys. While the precipitates are indeed crystalline, the measured lattice parameters differ slightly from their bulk counterparts, especially in the case of the Mn_2Ni_3Si phase. The combined SAXS/APT-XRD technique and analysis approach is by no means limited to studying precipitates in irradiated RPV steels, and it will also enormously contribute to characterization of relatively small fractions of otherwise unidentified nm-scale phases in a wide variety of other structural materials systems. The extension of this combined approach to other materials systems, as well including other relevant techniques, such as neutron small angle scattering and diffraction, will also be explored in the future.

V. ACKNOWLEDGMENTS

This work was carried out as part of a NEET project at BNL supported by the US Department of Energy, Office of Science, Nuclear Energy (DOE-NE). Funding was also provided by the DOE Nuclear Energy University Program. Use of the National Synchrotron Light Source, Brookhaven National Laboratory, was supported by the DOE under Contract No. DE-AC02-98CH10886. Use of the National Synchrotron Light Source-II, Brookhaven National Laboratory, was supported by the DOE under Contract No. DE-SC0012704. We acknowledge the Nuclear Scientific User Facilities (NSUF) and the Center for Advanced Energy Studies-Microscopy and Characterization Suite (CAES-MaCS) for carrying out the ATR irradiation as well as providing the use of facilities to perform post irradiation exami-

nation of the alloys.

VI. REFERENCES

REFERENCES

[1]G. R. Odette and G. E. Lucas, Radiat. Eff. Defects Solids **144**, 189 (1998).

[2]G. R. Odette, B. D. Wirth, D. J. Bacon, and N. M. Ghoniem, MRS Bulletin **26**, 176 (2001).

[3]G. R. Odette and G. E. Lucas, JOM **53**, 18 (2001).

[4]G. R. Odette, MRS. Symp. Proc. **373**, 137 (1995).

[5]G. R. Odette and B. D. Wirth, J. Nucl. Mater. **251**, 157 (1997).

[6]C. L. Liu, G. R. Odette, B. D. Wirth, and G. E. Lucas, Mater. Sci. Eng. A **238**, 202 (1997).

[7]M. K. Miller and K. F. Russell, J. Nucl. Mater. **371**, 145 (2007).

[8]G. R. Odette and R. K. Nanstad, JOM **61**, 17 (2009).

[9]M. K. Miller, K. A. Powers, R. K. Nanstad, and P. Efsing, J. Nucl. Mater. **437**, 107 (2013).

[10]P. B. Wells, T. Yamamoto, B. Miller, T. Milot, J. Cole, Y. Wu, and G. R. Odette, Acta Mater. **80**, 205 (2014).

[11]W. Xiong, H. Ke, R. Krishnamurthy, P. Wells, L. Barnard, G. R. Odette, and D. Morgan, MRS Commun. **4**, 101 (2014).

[12]K. P. Gupta, J. Phase Equilib. Diffus. **27**, 529 (2006).

[13]X. Yan, A. Grytsiv, P. Rogl, V. Pomjakushin, and X. Xue, J. Alloy. Compd. **469**, 152 (2009).

[14]J. Jaroszewicz, W. De Nolf, K. Janssens, A. Michalski, and G. Falkenberg, Anal. Bioanal. Chem. **391**, 1129 (2008).

[15]G. Artioli, in *Synchrotron Radiation*, edited by S. Mobilio, F. Boscherini, and C. Meneghini (Springer Berlin Heidelberg, 2015) pp. 319–336.

[16]F. Zhang, J. Ilavsky, G. G. Long, J. P. G. Quintana, A. J. Allen, and P. R. Jemian, Metall.Mater.Trans. A **41**, 1151 (2010).

[17]J. Ilavsky and P. R. Jemian, J. Appl. Crystallogr. **42**, 347 (2009).

[18]Y. Zhao, K. Lu, and K. Zhang, Phys. Rev. B **66**, 085404 (2002).

[19]Y. Zhao, H. Sheng, and K. Lu, Acta Mater. **49**, 365 (2001).

[20]E. J. Fasiska and G. A. Jeffrey, Acta Crystallogr **19**, 463 (1965).

[21]Mostly retained Fe austenite, and in some cases possibly a small amount of fcc Cu.

[22]A. Cervellino, C. Giannini, and A. Guagliardi, J. Appl. Crystallogr. **36**, 1148 (2003).

[23]D. Balzar, N. Audebrand, M. R. Daymond, A. Fitch, A. Hewat, J. I. Langford, A. Le Bail, D. Louer, O. Masson, C. N. McCowan, N. C. Popa, P. W. Stephens, and B. H. Toby, J. Appl. Crystallogr. **37**, 911 (2004).

[24]N. V. Y. Scarlett and I. C. Madsen, Powder Diffr. **21**, 278 (2006).

[25]The MAUD software package[34] was also used to cross-check and confirm the modified Rietveld results. Similar values (within error) for all refined parameters were obtained in both packages.

[26]D. L. Porter and E. L. Wood, J. Nucl. Mater. **83**, 90 (1979).

[27]E. I. Gladyshevskii, Sov. Powder Metall. Met. Ceram **1**, 262 (1962).

[28]L. L. Araujo, R. Giulian, D. J. Sprouster, C. S. Schnohr, D. J. Llewellyn, P. Kluth, D. J. Cookson, G. J. Foran, and M. C. Ridgway, Phys. Rev. B **78**, 094112 (2008).

[29]R. Giulian, L. L. Araujo, P. Kluth, D. J. Sprouster, C. S. Schnohr, B. Johannessen, G. J. Foran, and M. C. Ridgway, J. Appl. Phys. **105**, 044303 (2009).

[30]G. K. Rane, U. Welzel, S. R. Meka, and E. J. Mittemeijer, Acta Mater. **61**, 4524 (2013).

[31]The R_{wp} for the irradiated samples, without the inclusion of the Ni-Mn-Si phase, were found to be higher in value when compared to the unirradiated refinements (∼7-10). Including the extra phase resulted in lower R_{wp} values, almost identical to their unirradiated counterparts reported in table 3.

[32]R. Ngayam-Happy, C. S. Becquart, C. Domain, and L. Malerba, J. Nucl. Mater. **426**, 198 (2012).

[33]G. Bonny, D. Terentyev, A. Bakaev, E. Zhurkin, M. Hou, D. Van Neck, and L. Malerba, J. Nucl. Mater. **442**, 282 (2013).

[34]L. Lutterotti, S. Matthies, H. R. Wenk, A. S. Schultz, and J. W. Richardson, J. Appl. Phys. **81**, 594 (1997).

TABLE I. Nominal chemical compositions (wt.%) for the RPV samples.

Sample ID	Cu	Ni	Mn	Mo	P	C	Si	Fe + imp
LC	0.41	0.86	1.44	0.55	0.005	0.14	0.23	bal.
LD	0.38	1.25	1.38	0.55	0.005	0.19	0.23	bal.
LG	0.01	0.74	1.37	0.55	0.005	0.16	0.22	bal.
LH	0.11	0.74	1.39	0.55	0.005	0.16	0.24	bal.
LI	0.2	0.74	1.37	0.55	0.005	0.16	0.24	bal.
CM6	0.02	1.68	1.5	0.54	0.007	0.15	0.17	bal.

TABLE II. The precipitate sizes and volume fractions as determined from previous APT measurements[10] and the SAXS analysis.

Sample ID	Irr. size (APT) (nm)	f (APT) (%)	Irr. size (SAXS) (nm)	f (SAXS) (%)
LC	2.9	1.8	2.9 (0.5)	1.8
LD	3.9	2.1	4.0 (1.1)	2.4
LG	2.5	1.3	2.4 (0.5)	1.3
LH	2.7	1.5	2.7 (0.5)	1.4
LI	2.7	1.5	2.5 (0.4)	1.6
CM6	3.0	2.8	3.2 (1.5)	2.9

TABLE III. Refined parameters for the unirradiated samples from the Rietveld analysis. Space groups of phases are [1]Im$\bar{3}$m,[2]Pnma, [3]Fm$\bar{3}$m.

Sample ID	Phase ID	lattice parameter (Å)	Weight (%)	Size (nm)	micostrain (e_0)	R_{wp}
LC	Ferrite[1]	2.864 (0.001)	96.2 (0.2)	115.0 (16.6)	0.065 (0.003)	5.1
	Cemenitite[2]	5.077 (0.003), 6.750 (0.005), 4.518 (0.003)	2.1 (0.1)	37.9 (9.5)	-	
	Austenite[3]	3.593 (0.002)	1.8 (0.5)	14.1 (7.5)	-	
LD	Ferrite	2.864 (0.0001)	95.5 (0.2)	116.0 (15)	0.067 (0.002)	5.6
	Cemenitite	5.079 (0.002), 6.751 (0.003), 4.519 (0.002)	2.7 (0.1)	32.9 (5.5)	-	
	Austenite	3.593 (0.001)	1.8 (0.1)	17.2 (1.5)	-	
LG	Ferrite	2.865 (0.001)	96.2 (0.1)	149.3 (5.0)	0.062 (0.002)	5.1
	Cemenitite	5.079 (0.001), 6.752 (0.002), 4.518 (0.001)	2.4 (0.1)	69.9 (15.0)	-	
	Austenite	3.604 (0.011)	1.4 (0.1)	1.8 (0.8)	-	
LH	Ferrite	2.846 (0.001)	96.1 (0.3)	146.5 (25.0)	0.064 (0.002)	5.2
	Cemenitite	5.077 (0.002), 6.751 (0.003), 4.518 (0.002)	2.5 (0.1)	34.7 (5.5)	-	
	Austenite	3.601 (0.009)	1.4 (0.2)	1.9 (0.5)	-	
LI	Ferrite	2.865 (0.001)	96.4 (0.1)	157.6 (5.5)	0.061 (0.002)	5.1
	Cemenitite	5.078 (0.001), 6.750(0.002), 4.518 (0.002)	2.5 (0.1)	50.84 (9.2)	-	
	Austenite	3.611 (0.005)	1.2 (0.1)	3.6 (1.5)	-	
CM6	Ferrite	2.865 (0.001)	96.8 (0.2)	141.9 (8.0)	0.061 (0.003)	6.0
	Cemenitite	5.081 (0.006), 6.752 (0.011), 4.519 (0.006)	2.6 (0.2)	15.2 (4.0)	-	
	Austenite	3.599 (0.001)	0.6 (0.1)	17.8 (4.1)	-	

TABLE IV. Refined parameters for the irradiated samples from the Rietveld analysis. Space groups of phases are [1]Im$\bar{3}$m,[2]Pnma, [3]Fm$\bar{3}$m, [4]Fd$\bar{3}$m

Sample ID	Phase ID	lattice parameter (Å)	Weight (%)	Size (nm)	micostrain (e_0)	R_{wp}
LC	Ferrite[1]	2.865 (0.001)	95.7 (0.2)	82.4 (12.9)	0.077 (0.00155)	4.7
	Cemenitite[2]	5.076 (0.003), 6.752 (0.006), 4.526 (0.003)	2.5 (0.2)	36.3 (9.4)	-	
	Mn-Ni-Si [3]	11.329 (0.018)	1.8 (0.2)	2.9 (fixed)	-	
LD	Ferrite	2.865 (0.001)	94.1 (0.3)	81.9 (14.7)	0.083 (0.00267)	5.7
	Cemenitite	5.078 (0.002), 6.761 (0.003), 4.524 (0.003)	2.8 (0.2)	31.9 (6.6)		
	Austenite	3.591 (0.002)	1.1 (0.1)	9.6 (1.7)	-	
	Mn-Ni-Si[3]	11.612 (0.032)	2.1 (0.2)	4.0(fixed) -		
LG	Ferrite	2.865 (0.001)	95.7 (0.2)	120.9 (10.0)	0.065 (0.001)	4.7
	Cemenitite	5.078 (0.001), 6.755 (0.003), 4.524 (0.001)	2.4 (0.2)	48.1 (7.7)	-	
	Mn-Ni-Si[3]	11.268 (0.020)	1.3 (0.2)	2.4 (fixed)	-	
LH	Ferrite	2.864 (0.001)	95.3 (0.3)	80.3 (11.9)	0.079 (0.002)	5.4
	Cemenitite	5.076 (0.003), 6.752 (0.004), 4.524 (0.003)	2.9 (0.2)	33.9 (5.9)	-	
	Mn-Ni-Si[3]	11.224 (0.031)	1.4 (0.2)	2.7 (fixed)	-	
LI	Ferrite	2.864 (0.001)	95.5 (0.3)	102.5 (20.1)	0.110 (0.002)	7.0
	Cemenitite	5.075 (0.005),6.754 (0.006), 4.527 (0.006)	2.7 (0.2)	39.0 (5.0)		
	Mn-Ni-Si[3]	11.445 (0.040)	1.6 (0.1)	2.5 (fixed)	-	
CM6	Ferrite	2.865 (0.001)	93.8 (0.3)	112.0 (10.0)	0.069 (0.002)	4.9
	Cemenitite	5.075 (0.004), 6.756 (0.007), 4.523 (0.004)	2.2 (0.1)	37.8 (6.5)	-	
	Austenite	3.585 (0.002)	0.6 (0.2)	14.0 (2.7)	-	
	Mn-Ni-Si [4]	6.197 (0.027)	2.9 (0.2)	3.2 (fixed)	-	